The Flinders University of South Australia

ELECTRONIC STRUCTURE OF MATERIALS CENTRE

Energy-momentum structure of the krypton valence shell by electron-momentum spectroscopy

R. Nicholson, S.W. Braidwood, I.E. McCarthy, E. Weigold and M.J. Brunger

ESM-124

March 1996

Energy-momentum structure of the krypton valence shell by electron-momentum spectroscopy.

R. Nicholson, S.W. Braidwood, I.E. McCarthy, E. Weigold* and M.J. Brunger
Physics Department, The Flinders University of South Australia, GPO Box 2100,
Adelaide, South Australia, Australia, 5001.

Abstract: Momentum distributions and spectroscopic factors are obtained in a high-resolution electron-momentum spectroscopy study of krypton at 1000 eV. The shapes and relative magnitudes of the momentum profiles are in good agreement with the results of calculations made within the distorted-wave impulse approximation (DWIA) framework. The DWIA describes the relative magnitudes of the $4p$ and $4s$ manifolds as well as giving a good representation of the shapes of the respective $4p$ and $4s$ cross sections. Results for the momentum profiles belonging to excited $^2P^o$ and $^2S^e$ manifolds are also presented. Spectroscopic factors for transitions belonging to the $^2P^o$ and $^2S^e$ manifolds are assigned up to a binding energy of 42 eV. The spectroscopic factor for the lowest $4s$ transition is 0.51 ± 0.01, whereas that for the ground-state $4p$ transition is 0.98 ± 0.01. Comparisons of the present binding energies and spectroscopic factors are made against the results of several many-body calculations and photoelectron spectroscopy (PES) results. In addition we outline a new procedure, utilising the experimental $4p$ and $4s$ manifold cross sections, that provides information on possible initial state configuration interaction (ISCI) effects in krypton.

PACS #'s : 34.80Dp, 35.10Hn

---

* Permanent address: Institute of Advanced Studies, R.S. Phys. S.E., Australian National University, Canberra, ACT, Australia, 0200.

1 Introduction

The (e,2e) process, in which the momenta of the incident electron and two emitted electrons in an ionizing collision are completely determined, is capable of revealing a rich variety of information. Depending on the kinematics employed, it is possible to investigate in detail either the dynamics of the ionizing collision or to use the reaction to elucidate the structure of the target and the ion. For example, the (e,2e) reaction has been used to investigate final-state correlation effects between the continuum electrons. This has mainly focussed on post-collision interaction (PCI) effects in the ionization of inner shells resulting in the emission of Auger electrons, particularly the ionization of the $2p$ shell of argon [1-10]. The reaction has also been used to study the correlations between resonance and direct ionization amplitudes in the autoionizing region of helium [9, 11-21]. When used for structure determination, high energies and high momentum transfers are normally employed to ensure the "clean" knock-out of a target electron. This form of (e,2e) spectroscopy is commonly referred to as electron momentum spectroscopy (EMS). It has been reviewed extensively [22-26] and in this communication we report its application in the first multiparameter-technique EMS study of the satellite structure of the krypton valence shell.

In quite recent times the study of correlation satellites in ionization spectra of rare gas atoms has been the subject of renewed interest [27, 28]. There are at least three reasons for this:

(a) The advancement of theoretical and computational methods is now giving reliable results for pole strengths for the most prominent low-energy satellites [29-31].

(b) The experimental development of atomic and molecular physics at an increasing number of synchrotron radiation centres makes feasible photoionization studies of gases at low pressures with synchrotron radiation of variable energy [32].

(c) The measured relative magnitudes of satellites in EMS valence electron spectra are independent of the incident energy and target electron momentum, but sometimes differ from the corresponding PES values, which appear to be energy dependent even at high momentum [23].

Whereas there have been a large number of EMS and PES measurements and theoretical calculations for the valence electronic structure of neon, argon and xenon (see, for example, references [33] - [36] and references therein), the same cannot be said for krypton. The earliest EMS studies of correlation effects in the binding energy spectra of krypton were made by Weigold *et. al.* [37] and Fuss *et. al.* [38]. Both these studies suffered from the limited statistical accuracy inherent with single channel coincidence measurements and from coincident energy resolutions $\Delta E_{coin} \geq 2$ eV, which effectively "smeared out" the $4s$ valence satellite structure. Leung and Brion [39] also independently measured, in an EMS experiment, the $4p$ and $4s$ satellite structure of krypton but again this was a single channel measurement so that the statistical quality of their data was only fair. We note, however, that they [39] improved the energy resolution of their work so that $\Delta E_{coin} = 1.6$ eV (FWHM), which whilst being clearly superior to Fuss *et. al.* [38], was, in the context of resolving the $4s$ satellite structure, of only marginal quality. Indeed Leung and Brion [39] specifically called for a further measurement of the krypton inner valence shell, with better energy resolution and improved statistics, to better define the $4s$ satellite structures. The results of just such a study, which have been made possible by employing multiparameter techniques, are reported here. Note, at this point, that a preliminary report of some aspects of this work [40] is superseded by the present manuscript.

PES investigations have also found significant satellite structure for the krypton valence shell. In this regard we note the early study of Spears *et. al.* [41] and the more recent, extensive, investigations of Svensson *et. al.* [32] and Krause *et. al.* [27]. From a theoretical perspective Dyall and Larkins [42, 43] have applied their *frozen-core CI model* to calculate the satellite spectrum of krypton (amongst others) up to binding energies of 43 eV. More exact calculations for the $4p$ and $4s$ satellite states have been provided by Fronzoni *et. al.* [30] and Brosolo *et. al.* [44] who employed a two hole-one particle

(2h-1p) CI calculation scheme.

In the present work we report a 1000 eV EMS study of the valence electronic structure of krypton, up to a binding energy of 42 eV. Spectroscopic factors for transitions belonging to the $^2P^o$ and $^2S^e$ manifolds are assigned and results for the momentum profiles belonging to excited $^2P^o$ and $^2S^e$ manifolds are presented and discussed. Finally, a new technique in extracting initial state configuration interaction information is outlined and applied to the present, respective, $4p$ and $4s$ manifolds. The results of this analysis are also presented and discussed.

2 Experimental Methods

The present study was conducted with an electron-coincidence spectrometer. This electron-coincidence spectrometer and the techniques used in the present EMS investigation of the satellite structure of krypton have been described in some detail previously by McCarthy and Weigold [23,24] (to which the interested reader is referred for more information), and so we do not go into further detail here. We note however, our recent major upgrade in our data acquisition and computer control system. Specifically, the obsolete PDP-LSI 11/23 computer and its associated CAMAC control units were replaced by a PC 486D computer with a μ-ACE MCA card and a National Instruments LabPC + card. The benefits of this upgrade in terms of data handling, processing and storage and hardware reliability were manifest, in particular greatly reducing down time in the experiment.

The high purity krypton is emitted into the target chamber through a capillary tube, the leak rate being controlled by a variable leak valve. The collision region is surrounded by a chamber pumped by a 700ls^{-1} diffusion pump. Apertures and slits are cut in the collision chamber for the incident beam and ejected electrons. The differentially pumped collision region makes it possible to increase the target gas density by a factor of about two while keeping the background pressure in the spectrometer below 10^{-5} Torr. This allowed us to operate the electron beam at a lower current (typically $40\mu A$) resulting in a better energy resolution. The energy resolution of the present measurements is 1.25 eV

(FWHM), and the angular resolution is 1.2° (FWHM). Operating conditions were chosen so that the incident energy E_0 = 1000 eV + binding energy (ϵ_i), the ejected electrons had energies E_A and E_B in the range 500 ± 7 eV and made angles of $\theta_A = \theta_B = 45°$ with respect to the incident electron beam direction. The out-of-plane azimuthal angle ϕ was varied over the angular range 0 − 25° in order to vary the recoil momentum as

$$p = \left[(2p_A \cos\theta - p_0)^2 + 4p_A^2 \sin^2\theta \sin^2\frac{\phi}{2}\right]^{\frac{1}{2}}. \tag{1}$$

Binding energy spectra were taken at each out-of-plane azimuthal angle over the range $\epsilon_i = 9 - 42$ eV using the binning mode [22].

3 Orbital Manifolds

At energies of 1000 eV or higher the distorted-wave impulse approximation (DWIA) has given differential cross sections for noncoplanar symmetric ionization equivalent to the more detailed distorted-wave Born approximation (DWBA) [45]. Both give a good account of experimental data for the valence states of inert gases [23]. We treat the DWIA as an accurate description of the ionization reaction and use a statistical procedure to extract detailed structure information from the experiment.

The differential cross section in the DWIA is [23]

$$\frac{d^5\sigma}{d\Omega_f d\Omega_s dE_f} = (2\pi)^4 \frac{k_f k_s}{k_0} f_{ee} \Sigma_m$$

$$\times \left| \int d^3k_f \int d^3k_s \int d^3k_0 \langle \chi^{(-)}(\mathbf{k}_f)|\mathbf{k}_f\rangle \langle \chi^{(-)}(\mathbf{k}_s)|\mathbf{k}_s\rangle \langle \mathbf{q}i|0\rangle \langle \mathbf{k}_0|\chi^{(+)}(\mathbf{k}_0)\rangle \right|^2 \tag{2}$$

It has been written in this form to make explicit its dependence on the structure amplitude $\langle \mathbf{q}i|0\rangle$, where

$$\mathbf{q} = \mathbf{k}_f + \mathbf{k}_s - \mathbf{k}_0, \tag{3}$$

0 labels the ground state of the target atom and i labels the observed state of the residual ion. The subscripts 0, f, s refer to the incident and faster and slower outgoing electrons

respectively. The projection quantum number of magnetically-degenerate ion states is m. $|\chi^{(\pm)}(\mathbf{k})\rangle$ are elastic-scattering states calculated in the appropriate potential, which at the present energy is the spin-averaged static-exchange potential for the interaction of an electron with the appropriate system, i.e. the atom in the initial state, the ion in the final state. The electron-electron collision factor is usually taken to be the absolute square of the half-on-shell Coulomb t matrix [46], appropriately summed and averaged over spin states.

The initial and final bound states may be expanded in a configuration interaction representation based on a set of orthonormal orbitals β. The set β is conveniently chosen by a structure calculation of the target ground state. Here we use orbitals computed in the analytic potential of Green *et. al.*[47]. The structure amplitude may be calculated to arbitrary accuracy in this way, although relaxation effects in the ion make the expansion somewhat inefficient. The structure amplitude is sometimes called the Dyson orbital for the ion state i, since it is a one-electron quantity.

Great insight into structure is achieved by making the weak-coupling approximation [23] in which

$$\langle \mathbf{q}i|0\rangle = [S_i^\alpha]^{\frac{1}{2}} \phi_\alpha(\mathbf{q}), \tag{4}$$

where $\phi_\alpha(\mathbf{q})$ is the normalized Dyson orbital in momentum space and S_i^α is the spectroscopic factor for the state i. The weak-coupling approximation assigns ion states i to orbital manifolds α, the corresponding orbital manifold being identified by the characteristic momentum-profile shape

$$f(q) = \Sigma_m \left| \langle \chi^{(-)}(\mathbf{k}_f) \chi^{(-)}(\mathbf{k}_s)|\alpha \chi^{(+)}(\mathbf{k}_0)\rangle \right|^2. \tag{5}$$

It is justified by the fact, observed in all experiments to date on atoms or molecules, that the overwhelming majority of valence states have characteristic momentum profiles.

The normalized Dyson orbital is fully defined for all the states i in the manifold α by the spectroscopic sum rule

$$\Sigma_i S_i^\alpha = 1. \tag{6}$$

The orbital energy is given by

$$\epsilon_\alpha = \Sigma_i S_i^\alpha \epsilon_i. \tag{7}$$

The states i of an orbital manifold α are often called satellites of the orbital α.

Finally, note that the relevant DWIA differential cross sections, as given by equation (2), are all folded with the experimental angular resolution for comparison with the experimental data.

4 Experimental determination of normalized Dyson orbitals

For many atoms and molecules excellent agreement with experiment is obtained by assuming that the normalized Dyson orbital α is equivalent to the corresponding basis orbital β, which is very similar to the Hartree-Fock orbital. For occasional orbital manifolds, such as the one-state $1b_1$ manifold of H_2O[48], the Hartree-Fock orbital gives a very poor approximation, although the validity of the impulse approximation is confirmed by a detailed configuration interaction calculation of the Dyson orbital. In this case a much improved single-orbital calculation is achieved by density-functional methods [49]. It is therefore interesting to ask what orbital is defined by analysing experimental data for an orbital manifold by the distorted-wave-impulse and weak-coupling approximations.

In cases where the experimental criteria identify an orbital manifold the normalized Dyson orbital can be directly derived from the experimental momentum profile by an inverse-scattering procedure. The orbital α is represented as a linear combination of orthonormal basis orbitals β, which have the same symmetry as α, but different principal quantum numbers.

$$|\alpha\rangle = \sum_\beta c_{\alpha\beta}|\beta\rangle, \quad \alpha, \beta = 1, n. \tag{8}$$

The transformation matrix $\mathbf{C}$ is expressed in terms of a set θ of fitting parameters, chosen for experimental cross sections σ_α^μ at the data points $\mu \equiv (\hat{\mathrm{k}}_f, \hat{\mathrm{k}}_s)$ by minimizing the sum of weighted squares of the deviations

$$\sigma_\alpha^\mu = (2\pi)^4 \frac{k_f k_s}{k_0} F \int d\hat{\mathrm{k}} w_f(\hat{\mathrm{k}}, \hat{\mathrm{k}}_f) \int d\hat{\mathrm{k}}' w_s(\hat{\mathrm{k}}', \hat{\mathrm{k}}_s)$$
$$\times f_{ee} \Sigma_m |\langle \chi^{(-)}(\mathrm{k}) \chi^{(-)}(\mathrm{k}')| \alpha \chi^{(+)}(\mathrm{k}_0)\rangle|^2. \tag{9}$$

In spectroscopic experiments it is valid to consider the energies of the external electrons as well resolved, but to take into account angular resolution in the measurement of $\hat{\mathrm{k}}_f$ by integrating the cross section (2) over the solid angle $\hat{\mathrm{k}}$ with a normalized weight factor $w_f(\hat{\mathrm{k}}, \hat{\mathrm{k}}_f)$ and similarly for $\hat{\mathrm{k}}_s$. The experiment leaves one quantity undetermined. This is a constant normalization F, which is treated as an additional fitting parameter.

Using (8) we express (9) as

$$\sigma_\alpha^\mu = F \sum_{\beta\gamma} P_{\alpha,\beta\gamma} O_{\gamma\beta}^\mu = F \mathrm{tr}(\mathbf{P}_\alpha \mathbf{O}^\mu). \tag{10}$$

The density matrix $\mathbf{P}_\alpha$ for the orbital α is

$$P_{\alpha,\beta\gamma} = c_{\beta\alpha} c_{\alpha\gamma}. \tag{11}$$

The observation matrix $\mathbf{O}^\mu$ for the data point μ is

$$O_{\gamma\beta}^\mu = (2\pi)^4 \frac{k_f k_s}{k_0} \int d\hat{\mathrm{k}} w_f(\hat{\mathrm{k}}, \hat{\mathrm{k}}_f) \int d\hat{\mathrm{k}}' w_s(\hat{\mathrm{k}}', \hat{\mathrm{k}}_s) f_{ee} \Sigma_m$$
$$\times \langle \chi^{(-)}(\mathrm{k}) \chi^{(-)}(\mathrm{k}')| \gamma \chi^{(+)}(\mathrm{k}_0)\rangle \langle \chi^{(+)}(\mathrm{k}_0) \beta | \chi^{(-)}(\mathrm{k}') \chi^{(-)}(\mathrm{k})\rangle. \tag{12}$$

The parameter fitting is done by minimizing the quantity S, given by

$$S = \sum_\mu w_\mu [\sigma_\alpha^\mu - F \mathrm{tr}(\mathbf{P}_\alpha \mathbf{O}^\mu)]^2, \tag{13}$$

with respect to the set

$$a \equiv (F, \theta) \tag{14}$$

of fitting parameters. The fitting procedure determines the mean values and variances of the parameters a. The normalized weight w_μ of each data point μ is given by the inverse of the variance for μ.

The parameters θ are obtained by the requirement that the sets α and β of orbitals are orthonormal. This is equivalent to requiring the transformation matrix C to be unitary. The constraint is achieved by parametrizing the coefficients with the set of Jacobi-type planar rotation matrices $\mathrm{R}(\theta_j)$, which have the same dimension as C.

$$\mathbf{C} = \Pi_{j \neq \alpha} \mathbf{R}(\theta_j). \tag{15}$$

If all the parameters θ_j are zero then C is the unit matrix and the transformed orbitals are the basis orbitals.

With the present experimental data (see section 5 for more details on the experimental momentum distributions) the $4p$ and $4s$ normalized Dyson orbitals were determined from differential cross sections summed for the corresponding manifolds. Table 1 gives the four-dimensional bases, the coefficients $c_{\alpha\beta}$ and their standard deviations. Figures 1 and 2 show the comparison with experiment of differential cross sections calculated with the best-fit normalized Dyson orbitals and with the principal basis orbital.

The $4p$ orbital is determined to be the basis orbital within experimental error. For the $4s$ orbitals admixtures of $3s, 5s$ and $6s$ are statistically significant, the largest being $6s$. The determined orbital gives considerable improvement over the $4s$ basis orbital. The normalization factors F for the $4p$ and $4s$ orbitals are respectively, on the same arbitrary scale, 1.007 ± 0.009 and 1.000 ± 0.020.

5 Results and Discussion

(i) Binding-energy spectrum

The binding energy spectrum of krypton in the region $\epsilon_i \sim 9 - 42$ eV is shown in figures 3(a), (b) and (c), respectively, for a total energy of 1000 eV and with the out-of-plane azimuthal angles $\phi = 0°$ and $\phi = 8°$. Also shown in this figure is the summed spectrum for $\phi = 0° + 8°$. At $\phi = 0°$ the nominal momentum p ranges from 0.16 a.u. at the binding energy of the first peak ($\epsilon_i = 14.11$ eV) to 0.18 a.u. for $\epsilon_i = 40.47$ eV. At 8° the corresponding momenta are 0.61 a.u. and 0.62 a.u., respectively. Note that the

first peak in figure 3 is actually a convolution of the $J = \frac{3}{2}$ and $J = \frac{1}{2}$ components of the 4p line. However, as these spin-orbit split states are only separated by 0.67 eV, the coincident energy resolution of the present experiment did not allow the two components to be resolved. The spectra in figure 3 reproduce all the correlation satellites found by Brunger [40] in his preliminary study of the work we now report in full here.

Considering figure 3 in more detail then at $\phi = 0°$, i.e. at low momenta, the $4p$ ground-state cross section is some 48% of that for the main $4s^{-1}$ transition ($4s^1 4p^6$) at 27.52 eV, whereas at $\phi = 8°$ its cross section is $2\frac{1}{2}$ times that of the 27.52 eV transition. Thus any reasonable ^2P satellite intensity in the range 9-42 eV should be noticeable in figure 3 by peaks which are somewhat stronger at $\phi = 8°$ than at $\phi = 0°$. Although it is not immediately apparent from figure 3 we find that, aside from the main ($4s^2 4p^5$) $4p^{-1}$ line at $\epsilon_i = 14.11$ eV, the only other candidate[40] for membership of the ^2P manifold is peak 3 at $\epsilon_i = 30.25$ eV. On the other hand, satellites belonging to the ^2S manifold should have a much larger cross section at $\phi = 0°$ compared to that at $\phi = 8°$. Peak 2 and peaks 4-11 of figure 3 clearly correspond to this behaviour.

In attempting to assign configurations for the transitions 1-11 of figure 3 we made use of the calculations of Dyall and Larkins [42,43] and Fronzoni *et. al.*[30], as well as the PES results of Svensson *et. al.*[32] and Krause *et. al.*[27] and the optical data of Moore[50]. A summary of our classifications for the final-state configurations of the ^2S and ^2P manifolds of Kr, that we observed, and the spectroscopic factors derived from the present EMS momentum distributions, that we consider in detail in part (ii) of this section, are given in table 2. We note that the spectroscopic factors for final states belonging to the $4p$ and $4s$ manifolds can in principle not only be obtained, as we did here, from the momentum distributions but, as was done by Brunger [40], they can also be derived from the relative intensities obtained from the binding energy spectra. As we believe the present procedure for determining the S_i^α is more exact than that used by Brunger[40], the current results (see table 2) supersede those of Brunger, although both sets are consistent to within their respective stated uncertainties. Also shown in table 2 are the PES results of Svensson *et. al.*[32] and Krause *et. al.*[27], the earlier EMS result of Fuss *et. al.*[38] and Leung and Brion[39], and the calculated results of Dyall and Larkins[42, 43], Fronzoni *et. al.*[30] and Brosolo *et. al.*[44]. Note, as Amusia and Kheifets [29] found that the PES cross section was not proportional to the spectroscopic factor we would, a priori, not expect to find a significant correspondence between the EMS and PES results for S_i^α.

(ii) Momentum Distributions

Binding-energy spectra similar to those shown in Fig. 3 were taken at a range of azimuthal angles. The energy range at each angle and the angular range itself were stepped through repeatedly. Each part of each spectrum at every angle was scanned sequentially for an equal time, each run consisting of many scans. The spectra were then used to obtain cross sections to selected final ion states relative to each other as a function of ϕ or momentum p [Eq.(1)]. In some case neighbouring final ion states could not be completely resolved e.g. peak 11 of figure 3; where this occurred, they were then grouped under single peaks.

The measured (e,2e) cross sections (or momentum distributions) are not absolute, but relative normalizations are maintained. The present momentum distributions are normalized to the DWIA by equating the measured intensity at $\phi = 8°$ in the $4p$ ground-state transition to 0.98× DWIA at that point. This is shown in the upper plot of figure 4 where we see agreement between the current experiment and DWIA momentum distribution is excellent over the entire range of measured momentum. The normalization of 0.98 was chosen to allow for 2% of the $4p$ intensity for line 3. This is shown in the lower plot of figure 4. Clearly, nearly all the $4p$ strength goes to the ground-state transition so that we can assign the spectroscopic factor for this transition to be 0.980 ± 0.005. Note again, as just described above, we have taken this into account in the normalization of the current data.

Figure 5 shows that the DWIA cross section for the $4s$ manifold is, to within the statistical uncertainties on the current measurement, in quite good agreement with the measured $4s$ manifold cross section in terms of both shape and magnitude over the whole angular range of this experiment, although we note that our earlier analysis, as discussed in section 4 and represented by Fig. 2, suggested that an even better fit can be obtained if some initial state configuration interaction is allowed for. Nonetheless the result given in figure 5 shows that essentially all of the $4s$ strength has been observed in the measurement over the range $\epsilon_i = 27 - 42$ eV. Nearly all the strength in this region belongs to the $4s$ manifold; the small $4p$ strength which is observed and discussed next is not included in the $4s$ manifold cross section shown in the figure.

Considering the lower frame of figure 4 in more detail (i.e. the momentum distribution for line 3 in Fig. 3) then we find quite good agreement is obtained between the present EMS data and the $4p$ - DWIA momentum distribution, within the errors on the data, when the latter is scaled by a factor of 0.02. The exception to this is at $\phi = 8°$ where both of the current EMS measurements are lower in magnitude than that predicted by the appropriately scaled calculation. In light of this, the earlier observation of McCarthy *et. al.*[34] in argon and the fact (see table 2) that Krause *et. al.*[27] saw several transitions of ^2D symmetry in close proximity to this correlation satellite at $\epsilon_i = 30.25$ eV, we investigated the possibility that the present momentum distribution was in fact indicative of a pole of ^2D manifold symmetry. However, after calculation of the appropriate $4d$-state DWIA result and our comparison of it to our experimental momentum distribution of the lower frame of figure 4, this possibility can be largely discounted.

The shape of the 27.52 eV transition (line 2 of Fig. 3) is virtually indistinguishable from the $4s$ manifold cross section. It is also in quite satisfactory agreement with the DWIA calculation when the calculated $4s$ manifold cross section is multiplied by a factor 0.510, as illustrated in the upper frame of Fig. 6. Thus the spectroscopic factor for this transition is 0.510 and the 27.52 eV state, with a dominant configuration of $4s^14p^6$, contains 51% of the $4s$ pole strength. In the lower frame of Fig. 6 we show the momentum profile for the $\epsilon_i = 32.09$ eV $4s^24p^4(^1S)5s\ ^2S$ correlation satellite (line 4 of Fig. 3). Again, there is rather good agreement for the shape of this transition and that of the $4s$ manifold. Also, it is in good agreement, to within the experimental uncertainties on the data, with the DWIA calculation when the calculated $4s$ manifold cross section is multiplied by a factor of 0.075. We note that, in principle, given our coincident energy resolution, a contribution to our measured momentum distribution from the PES observed odd-parity state $4s^24p^4(^1D)5p\ ^2P_{\frac{3}{2},\frac{1}{2}}$ at $\epsilon_i = 32.61$ eV, could occur. However, the excellence of the fit of the present momentum distribution at 32.09 eV to the $4s^{-1}$ DWIA calculation suggests that any contribution of the odd-parity state must be small ($< 0.005\ 4p$). This latter observation is consistent with the calculation of Dyall and Larkins [42,43] who found that the $4s^24p^4(^1S)5s\ ^2S$ transition was twice as strong as the $4s^24p^4(^1D)5p\ ^2P_{\frac{3}{2},\frac{1}{2}}$ transition, although we note that contrary to this the $2h-1p$ calculation [30,44] predicted precisely the inverse result.

Figure 7 (upper frame) gives the momentum profile for the $\epsilon_i = 33.98$ eV, $4s^2\,4p^4(^1D)4d\,^2S$ correlation satellite (line 5 of Fig. 3). The shape of the 33.98 eV transition is, within experimental error, essentially indistinguishable from the $4s$ manifold cross section and, on comparison with the DWIA calculation, when scaled by a factor of 0.202, good agreement is obtained for the magnitude of the cross section. The lower frame of Fig. 7 shows the momentum distribution for line 6 of Fig. 3. This is quite a weak satellite and as discussed in Brunger[40] there was some controversy between the PES classification of Svensson et. al.[32], on the one hand, and Krause et.al.[27], on the other, for the configuration of this line. When the present DWIA result for the $4s$ manifold is scaled by a factor of 0.029 it is in fair agreement with the present EMS measurements for all the ϕ of the current investigation. The shape is completely inconsistent with a possible $4p$ transition. Consequently we conclude, largely in support of the configuration proposed by Krause et. al.[27], that the dominant configuration at $\epsilon_i = 34.47$ eV is $4s^24p^4(^1S)6s\ ^2S$. Note that the present EMS determination can not rule out entirely a very small ^2P contribution due to the $4s^24p^4(^3P)6p$ transition at this binding energy, but such a contribution must be small ($< 0.005\ 4p$). Further support for this proposition is provided by the calculation of Dyall and Larkins[42,43] who found that the spectroscopic strength for the $4s^24p^4(^1S)6s\ ^2S$ line was over 6 times stronger than that for the $4s^24p^4(^3P)6p\ ^2P$ line (see table 2).

The current momentum distribution for line 7 of Fig. 3 is given in the upper frame of Fig. 8. The PES results of Svensson et. al.[32] and Krause et. al.[27] suggested that two possible configurations were to be found at the relevant binding energy of $\epsilon_i = 36.47$ eV. The first is an even-parity state of configuration: $4s^24p^4(^1D)5d\ ^2S$, while the second is an odd-parity state with classification $4s^2\ 4p^4(^1D)6p\ ^2P$. It is apparent from the upper frame of Fig. 8 that the present momentum distribution is in good agreement with the result of our $4s$ manifold DWIA calculation when the DWIA is scaled by a factor of 0.100. Clearly this result is indicative of this correlation satellite being both quite strong in intensity and being dominated by the $4s^24p^4(^1D)5d\ ^2S$ configuration. This observation, once again, does not necessarily mean that a contribution from the $4s^24p^4(^1D)6p\ ^2P$ transition is not occurring at $\epsilon_i = 36.47$ eV, although clearly such a contribution must be small (< 0.005).

Considering the lower frame of Fig. 8 we see the experimental momentum distribution for the $\epsilon_i = 37.81$ eV $4s^24p^4(^1D)6d\ ^2S$ satellite (line 8 of Fig. 3). Again there is quite good agreement for the shape of this transition and that of the $4s$ manifold. Also, it is in fair agreement with the DWIA calculation when the calculated $4s$ manifold cross section is multiplied by a factor of 0.027, particularly when one allows for the uncertainties on the respective experimental data points.

In figures 9 and 10 we present the experimental momentum distributions for the series of final-ion state $4s^24p^4(^1D)nd\ ^2S$ with $n = 7, 8, 9, 10\ldots$, at the respective binding energies $\epsilon_i = 38.57, 39.21$ and 40.47 eV. We note that these transitions correspond to lines 9, 10 and 11 in the binding energy spectra of Fig. 3. Each of these respective transitions can clearly be classified as belonging to the ^2S manifold, although we acknowledge that there is perhaps more scatter in their experimental momentum distribution data points than was observed earlier for the lower binding energy states. Nonetheless agreement between them and our appropriately scaled DWIA $4s$ manifold cross section is at worst fair in each case, these relevant scaling factors or spectroscopic factors being found either in Table 2 or on the respective figures.

6 Conclusions

EMS measurements at 1000 eV have been made for transitions to excited states of Kr^+. The momentum profiles and cross sections relative to the ground-state $4p^{-1}$ transition are well described by the distorted-wave impulse approximation. Detailed spectroscopic-factor determinations have been obtained for the $4p$ and $4s$ manifolds. The main $4s$ transition at $\epsilon_i = 27.52$ eV has a spectroscopic strength of 0.510. This is in quite good agreement with the most recent $2h-1p$ configuration-interaction scheme calculations of Fronzoni *et. al.*[30] and Brosolo *et. al.*[44]. Spectroscopic factors for the $4s$ manifold were suitably determined by comparing our experimental cross sections to our appropriately scaled DWIA results, the sum of the different $4s$ components giving the correct $4s$ manifold cross section normalized relative to the $4p$ cross section.

The present measurements reveal some small 4p strength at a higher binding energy in the binding-energy spectrum. They confirm that the $4p^{-1}$ ground-state transition is almost a pure one-hole transition with a spectroscopic factor of 0.980 ± 0.005.

Finally, we have applied a new inverse-scattering technique to the experimental $4s$ and $4p$ momentum distributions in order to probe initial-state configuration interaction effects. We found that the $4p$ orbital was determined to be the basis orbital to within experimental error, while the $4s$ orbital had a statistically significant admixture of $3s, 5s$ and particularly $6s$ configurations.

7 Acknowledgements

We are grateful to the Australian Research Council (ARC) for their partial financial support of this work and to Ms. P. Dall'Armi for supplying the krypton. M. Brunger also thanks the ARC for his QE2 Fellowship while R. Nicholson acknowledges the Flinders University of South Australia for his scholarship. Ian McCarthy is grateful to Marilyn Mitchell for attempting to read his writing.

References

[1] E.C. Sewell and A. Crowe, J. Phys. B **15**, L357 (1982).

[2] E.C. Sewell and A. Crowe, J. Phys. B **17**, 2913 (1984).

[3] W. Sandner and M. Völkel, J. Phys. B **17**, L597 (1984).

[4] G. Stefani, L. Avaldi, A. Lahmann-Bennani and A. Duguet, J. Phys. B **19**, 3787 (1986)

[5] B. Lohmann, J. Phys. B **24**, L249 (1991).

[6] B. Lohmann, X-K. Meng and M. Keane, J. Phys. B **25**, 5223 (1992).

[7] D.K. Waterhouse, J.H. Flexman and J.F. Williams, "Abstracts 18th ICPEAC" (Aarhus University: Aarhus), 212 (1993).

[8] S. Bell, P. Johnson and B. Lohmann, "Abstracts 18th ICPEAC" (Aarhus University: Aarhus), 213 (1993).

[9] M-Y. Kuchiev and S.A. Sheinerman, J. Phys. B **27**, 2943 (1994).

[10] D.K. Waterhouse, J.H. Flexman and J.F. Williams, "Abstracts 19th ICPEAC" (Whistler: British Columbia), 239 (1995).

[11] E. Weigold, A. Ugbabe and P.J.O. Teubner, Phys. Rev. Lett. **35**, 209 (1975).

[12] A. Pochat, R.J. Tweed, M. Doritch and J. Peresse, J. Phys. B **15**, 2269 (1982).

[13] M-Y. Kuchiev and S.A. Sheinerman, Sov. Phys. Usp. **32**, 569 (1989).

[14] J. Lower and E. Weigold, J. Phys. B **23**, 2819 (1990).

[15] D.G. McDonald and A. Crowe, Z. Phys. D **23**, 371 (1992).

[16] D.G. McDonald and A. Crowe, J. Phys. B **26**, 2887 (1993).

[17] I.E. McCarthy and B. Shang, Phys. Rev. A **47**, 4807 (1993).

[18] A. Kheifets, J. Phys. B **26**, 2053 (1993).

[19] O. Samardzic, J. Hurn, E. Weigold and M.J. Brunger, Aust. J. Phys. **47**, 703 (1994).

[20] O. Samardzic, A.S. Kheifets, E. Weigold, B. Shang and M.J. Brunger, J. Phys. B **28**, 725 (1995).

[21] A. Crowe, D.G. McDonald, S.E. Martin and V.V. Balashov, "AIP Conference Proceedings: XIXth ICPEAC" (AIP Press: New York), in press (1995).

[22] I.E. McCarthy and E. Weigold, Rep. Prog. Phys. **51**, 299 (1988).

[23] I.E. McCarthy and E. Weigold, Rep. Prog. Phys. **54**, 789 (1991).

[24] I.E. McCarthy and E. Weigold, "Electron-Atom Collisions" (Cambridge University Press: Cambridge) (1995).

[25] C.E. Brion, "Proc. 18th ICPEAC" (AIP Press: New York), 350 (1993).

[26] M.A. Coplan, J.H. Moore and J.P. Doering, Rev. Mod. Phys. **66**, 985 (1994).

[27] M.O. Krause, S.B. Whitfield, C.D. Caldwell, J-Z. Wu, P. van der Meulen, C.A. de Lange and R.W.C. Hansen, J. Elect. Spectrosc. Relat. Phenom. **58**, 79 (1992).

[28] M. Pahler, C.D. Caldwell, S.J. Schaphorst and M.O. Krause, J. Phys. B. **26**, 1617 (1993).

[29] M. Ya. Amusia and A. Kheifets, Aust. J. Phys. **44**, 293 (1991).

[30] G. Fronzoni, G. De Alti, P. Decleva and A. Lisini, J. Elect. Spectrosc. Relat. Phenom **58**, 375 (1992).

[31] A. Kheifets, J. Phys. B **28**, in press (1995).

[32] S. Svensson, B. Eriksson, N. Martensson, G. Wendin and U. Gelius, J. Elect. Spectrosc. Relat. Phenom. **47**, 327 (1988).

[33] O. Samardzic, S.W. Braidwood, E. Weigold and M.J. Brunger, Phys. Rev. A **48**, 4390 (1993).

[34] I.E. McCarthy, R. Pascual, P. Storer and E. Weigold, Phys. Rev. A **40**, 3041 (1989).

[35] S.W. Braidwood, M.J. Brunger and E. Weigold, Phys. Rev. A **47**, 2927 (1993).

[36] M.J. Brunger, S.W. Braidwood, I.E. McCarthy and E. Weigold, J. Phys. B **27**, L597 (1994).

[37] E. Weigold, S.T. Hood and I.E. McCarthy, Phys. Rev. A **11**, 566 (1975).

[38] I. Fuss, R. Glass, I.E. McCarthy, A. Minchinton and E. Weigold, J. Phys. B **14**, 3277 (1981).

[39] K.T. Leung and C.E. Brion, Chem. Phys. **82**, 87 (1983).

[40] M.J. Brunger, Aust. J. Phys. **48**, in press (1995).

[41] D.P. Spears, H.J. Fischbeck and T.A. Carlson, Phys. Rev. A **9**, 1603 (1974).

[42] K.G. Dyall and F.P. Larkins, J. Phys. B **15**, 203 (1985).

[43] K.G. Dyall and F.P. Larkins, J. Phys. B **15**, 219 (1985).

[44] M. Brosolo, P. Decleva, G. Fronzoni and A. Lisini, J. Mol. Struct. (Theochem.) **26**, 233 (1992).

[45] D.H. Madison, I.E. McCarthy and X. Zhang, J. Phys. B **22**, 2041 (1989).

[46] W.F. Ford, Phys. Rev. B **133**, 1616 (1964).

[47] A.E.S. Green, D.L. Sellin and A.S. Zachor, Phys. Rev. **184**, 1(1969).

[48] A.O. Bawagan, C.E. Brion, E.R. Davidson and D. Feller, Chem. Phys. **113**, 19 (1984).

[49] P. Duffy, D.P. Chong, M.E. Casida and D.R. Salahub, Phys. Rev. A **50**, 4707, (1994).

[50] C.A. Moore, "Atomic Energy Levels" Vol. 1-3, NBS Circular # 467 (Washington: U.S. Gov. Printing Office) (1971).

Figure Captions

Figure 1: Comparison of the present EMS $4p$ momentum distribution ($\bullet$) with those calculated within the DWIA for the best-fit normalised Dyson orbitals (—) and the principal Hartree-Fock orbital (- - -).

Figure 2: Comparison of the present EMS $4s$ manifold momentum distribution ($\bullet$) with those calculated within the DWIA for the best-fit normalised Dyson orbitals (—) and the principal Hartree-Fock orbital (- - -).

Figure 3: The 1000 eV noncoplanar symmetric EMS binding-energy spectra at (a) $\phi = 0^\circ$, (b) $\phi = 8^\circ$ and (c) $\phi = 0^\circ + 8^\circ$. The curves show the fitted spectra using the known energy-resolution function.

Figure 4: The upper frame shows the momentum distribution for the $4p$ ground-state $4s^2 4p^5\ {}^2P$ satellite, while the lower frame gives the momentum distribution for the $4s^2 4p^4(^3P)4d\ {}^2P$ correlation satellite at $\epsilon_i = 30.25$ eV. In both cases the present EMS measurements are denoted by ($\bullet$) and ($\Box$), while the appropriately scaled DWIA result is given by (—).

Figure 5: The 1000 eV noncoplanar symmetric momentum distribution for the total ${}^2S$ manifold of krypton. The present EMS results ($\bullet$) and ($\Box$) are compared to the result of our DWIA calculation (—).

Figure 6: The upper frame shows the momentum distribution for the $4s$ ground-state $4s^1 4p^6\ {}^2S$ satellite, while the lower frame give the momentum distribution for the $4s^2 4p^4(^1S)5s\ {}^2S$ correlation satellite at $\epsilon_i = 32.09$ eV. In both cases the present EMS measurements are denoted by ($\bullet$) and ($\Box$), while the appropriately scaled DWIA result is given by (—).

Figure 7: The upper frame shows the momentum distribution for the $4s^2 4p^4(^1D)4d\ {}^2S$ correlation satellite at $\epsilon_i = 33.98$ eV, while the lower frame gives the momentum distribution for the $4s^2 4p^4(^1S)6s\ {}^2S$ correlation satellite at $\epsilon_i = 34.47$ eV. In both cases the present EMS measurements are denoted by ($\bullet$) and ($\Box$), while the appropriately scaled DWIA result is given by (—).

Figure 8: The upper frame shows the momentum distribution for the $4s^2 4p^4(^1D)5d\ {}^2S$ correlation satellite at $\epsilon_i = 36.47$ eV, while the lower frame gives the momentum distribution for the $4s^2 4p^4(^1D)6d\ {}^2S$ correlation satellite at $\epsilon_i = 37.81$ eV. In both cases the present EMS measurements are denoted by ($\bullet$) and ($\Box$), while the appropriately scaled DWIA result is given by (—).

Figure Captions (continued)

Figure 9: The upper frame shows the momentum distribution for the $4s^2 4p^4(^1D)7d\ {}^2S$ correlation satellite at $\epsilon_i = 38.57$ eV, while the lower frame gives the momentum distribution for the $4s^2 4p^4(^1D)8d\ {}^2S$ correlation satellite at $\epsilon_i = 39.21$ eV. In both cases the present EMS measurements are denoted by ($\bullet$) and ($\Box$), while the appropriately scaled DWIA result is given by (—).

Figure 10: Momentum distribution for the $4s^2 4p^4(^1D)nd\ {}^2S$ correlation satellites ($n = 9, 10, \ldots$), grouped under the single peak with centroid binding energy $\epsilon_i = 40.47$ eV. The present EMS data ($\bullet$) and ($\Box$), are compared against an appropriately scaled DWIA result (—).

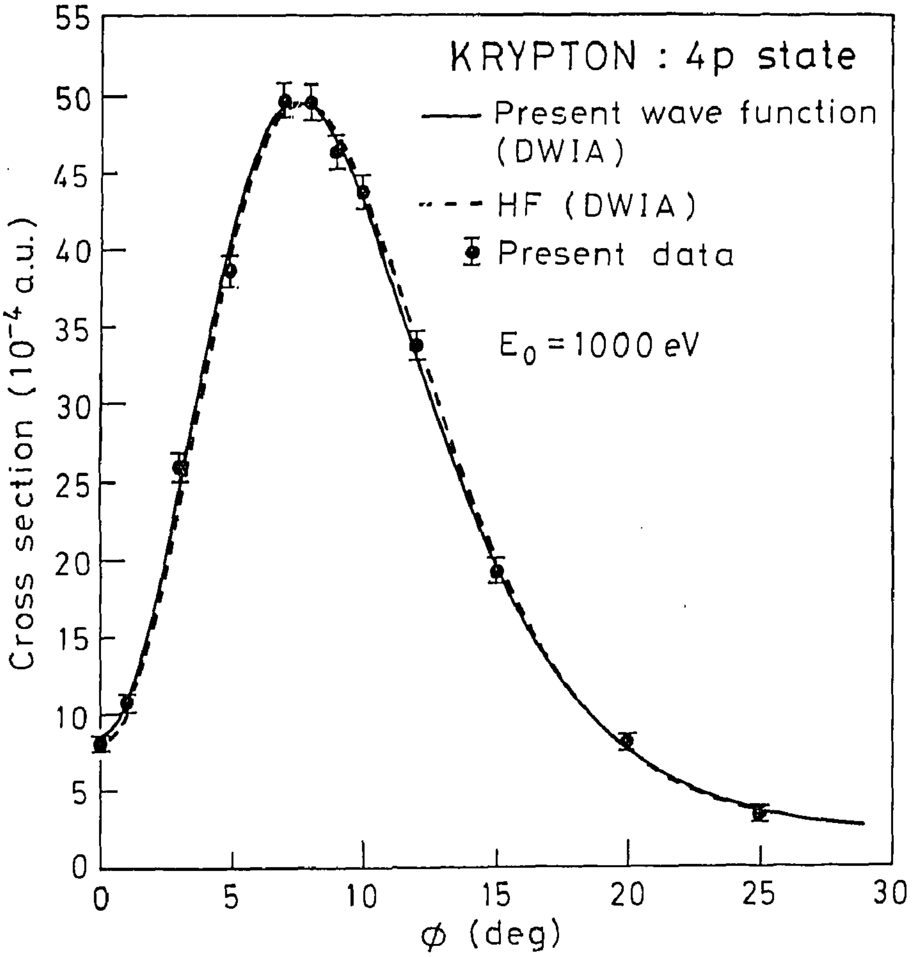
KRYPTON : 4p state
Present wave function (DWIA)
HF (DWIA)
Present data
$E_0 = 1000$ eV
Cross section (10^{-4} a.u.)
ϕ (deg)
0
5
10
15
20
25
30
35
40
45
50
55
0
5
10
15
20
25
30

Fig. 1

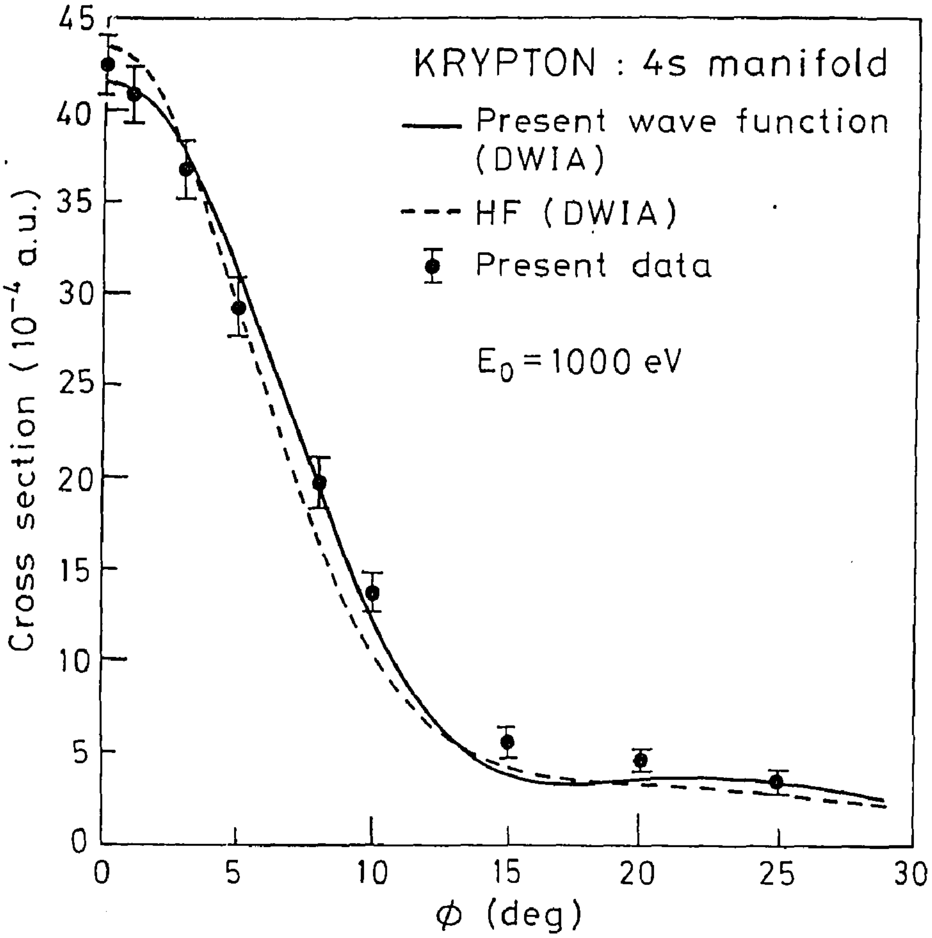
KRYPTON : 4s manifold
Present wave function (DWIA)
HF (DWIA)
Present data
$E_0 = 1000$ eV
Cross section (10^{-4} a.u.)
ϕ (deg)
0
5
10
15
20
25
30
35
40
45
0
5
10
15
20
25
30

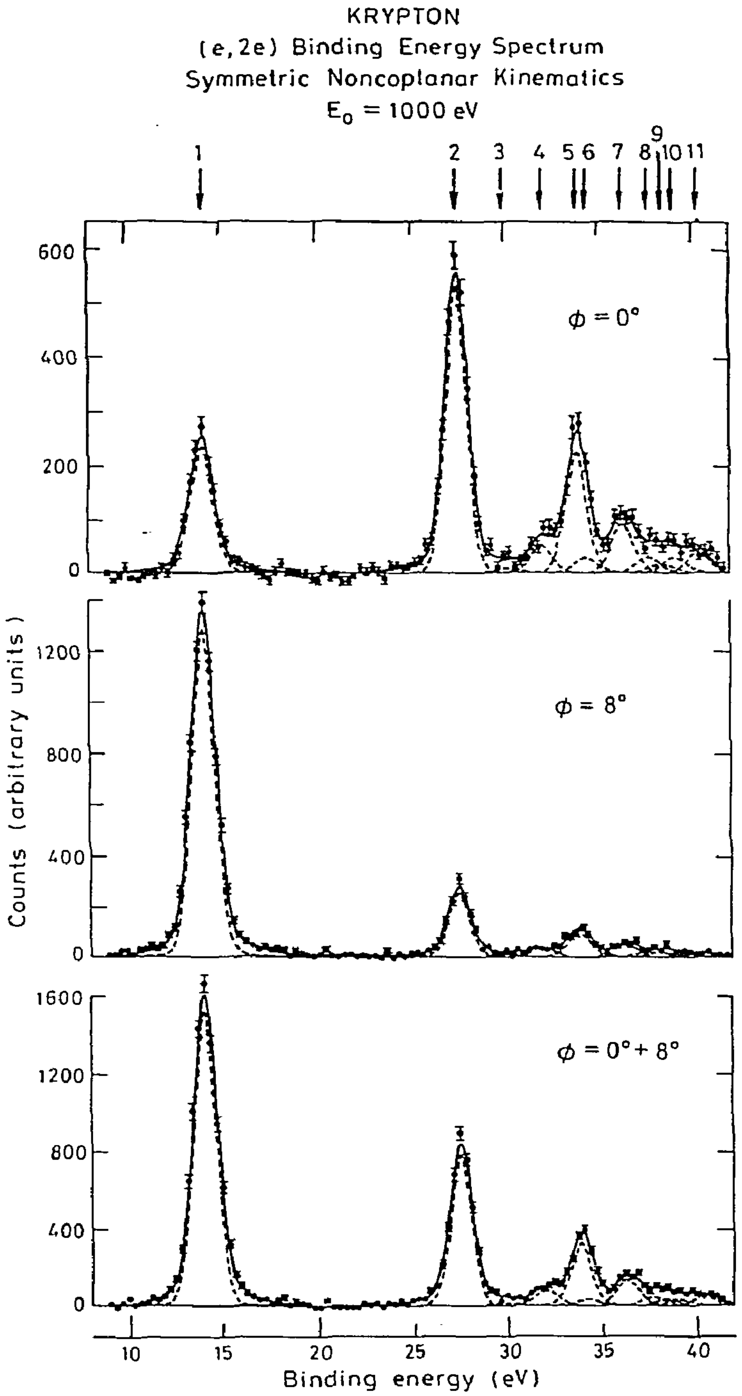
KRYPTON
(e,2e) Binding Energy Spectrum
Symmetric Noncoplanar Kinematics
E_0 = 1000 eV
1
2
3
4
5
6
7
8
9
10
11
600
400
200
0
ϕ = 0°
1200
800
400
0
ϕ = 8°
1600
1200
800
400
0
ϕ = 0° + 8°
Counts (arbitrary units)
10
15
20
25
30
35
40
Binding energy (eV)

Fig.3

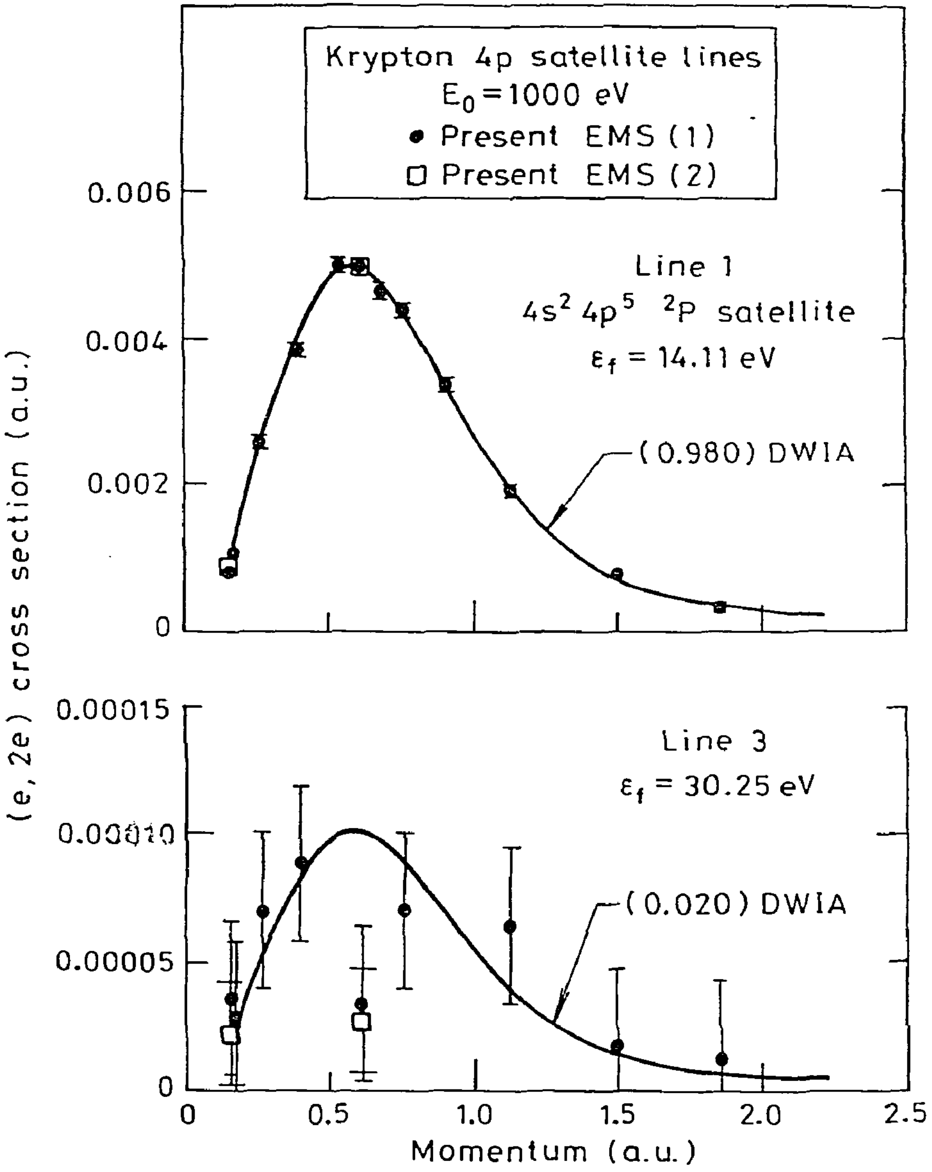
Krypton 4p satellite lines
E_0=1000 eV
● Present EMS (1)
□ Present EMS (2)
0.006
0.004
0.002
0
Line 1
$4s^2\,4p^5\ ^2P$ satellite
ε_f = 14.11 eV
(0.980) DWIA
(e, 2e) cross section (a.u.)
0.00015
0.00010
0.00005
0
Line 3
ε_f = 30.25 eV
(0.020) DWIA
0
0.5
1.0
1.5
2.0
2.5
Momentum (a.u.)

Fig.4

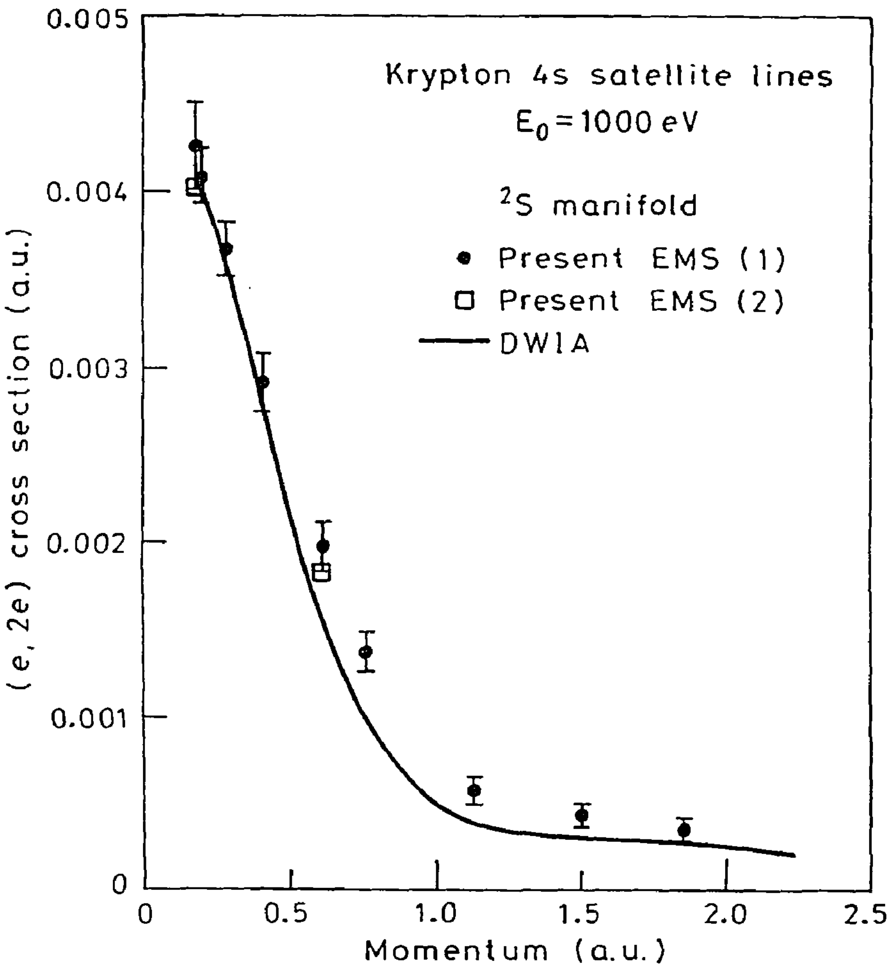
Krypton 4s satellite lines
$E_0 = 1000$ eV
^{2}S manifold
● Present EMS (1)
☐ Present EMS (2)
DWIA
(e, 2e) cross section (a.u.)
0.005
0.004
0.003
0.002
0.001
0
0
0.5
1.0
1.5
2.0
2.5
Momentum (a.u.)

Fig. 5

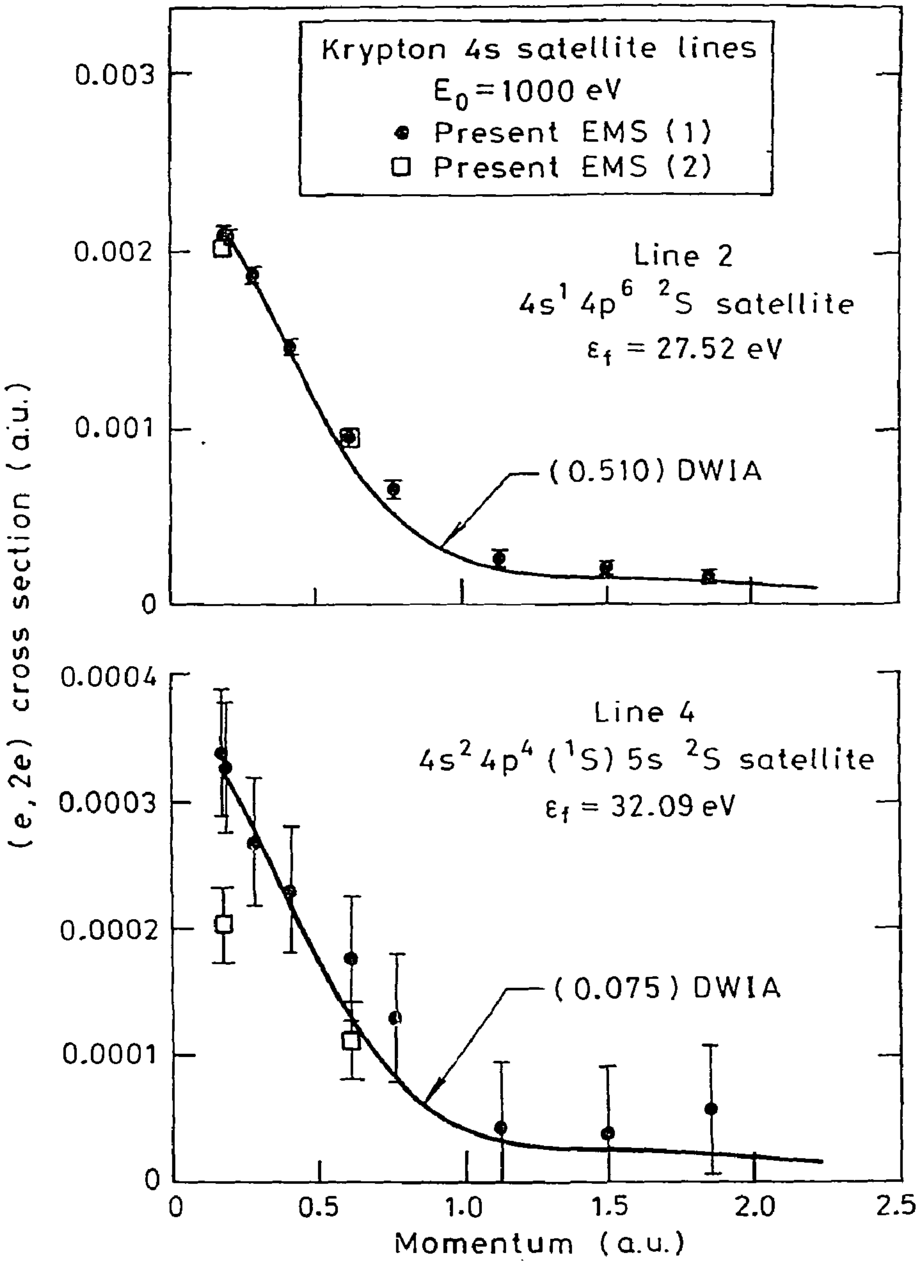
Krypton 4s satellite lines
$E_0 = 1000$ eV
● Present EMS (1)
☐ Present EMS (2)
Line 2
$4s^1 4p^6\ ^2S$ satellite
$\varepsilon_f = 27.52$ eV
(0.510) DWIA
Line 4
$4s^2 4p^4 (^1S) 5s\ ^2S$ satellite
$\varepsilon_f = 32.09$ eV
(0.075) DWIA
(e, 2e) cross section (a.u.)
0.003
0.002
0.001
0
0.0004
0.0003
0.0002
0.0001
0
0
0.5
1.0
1.5
2.0
2.5
Momentum (a.u.)

Fig. 6

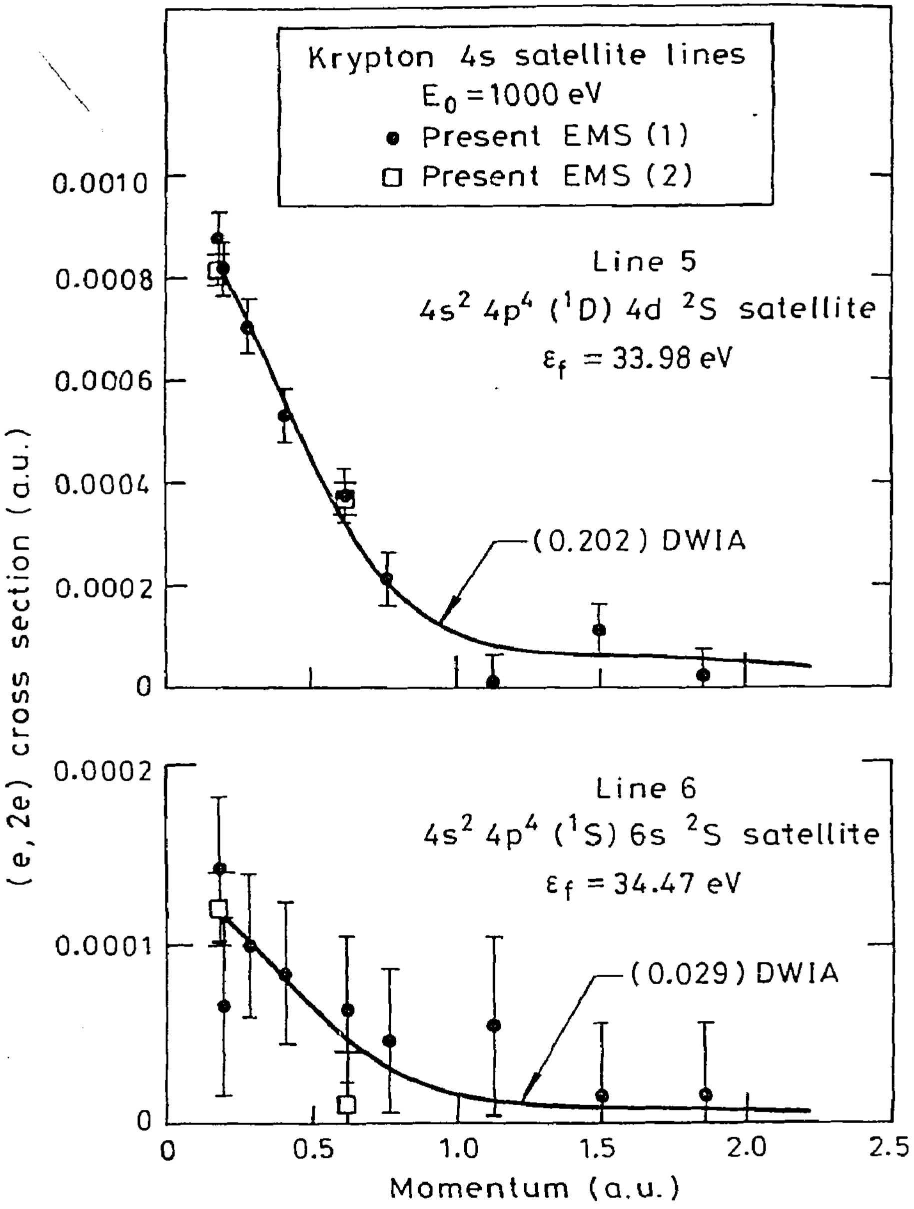
Krypton 4s satellite lines
$E_0 = 1000$ eV
● Present EMS (1)
□ Present EMS (2)
Line 5
$4s^2 4p^4 (^1D) 4d\ ^2S$ satellite
$\varepsilon_f = 33.98$ eV
(0.202) DWIA
Line 6
$4s^2 4p^4 (^1S) 6s\ ^2S$ satellite
$\varepsilon_f = 34.47$ eV
(0.029) DWIA
0.0010
0.0008
0.0006
0.0004
0.0002
0
0.0002
0.0001
0
0
0.5
1.0
1.5
2.0
2.5
(e, 2e) cross section (a.u.)
Momentum (a.u.)

Fig. 7

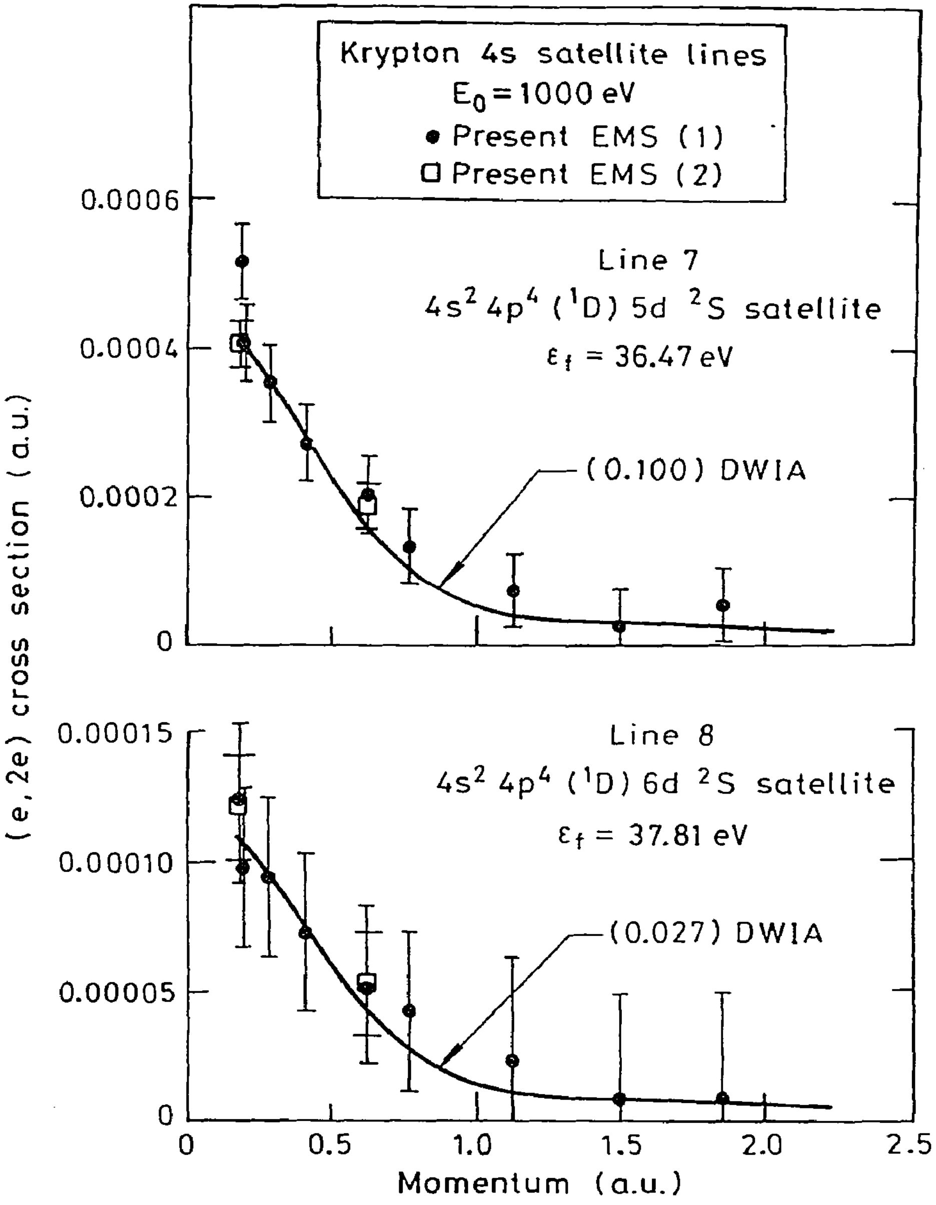
Krypton 4s satellite lines
$E_0 = 1000$ eV
● Present EMS (1)
□ Present EMS (2)
Line 7
$4s^2 4p^4 (^1D) 5d\ ^2S$ satellite
$\varepsilon_f = 36.47$ eV
(0.100) DWIA
Line 8
$4s^2 4p^4 (^1D) 6d\ ^2S$ satellite
$\varepsilon_f = 37.81$ eV
(0.027) DWIA
0.0006
0.0004
0.0002
0
0.00015
0.00010
0.00005
0
0
0.5
1.0
1.5
2.0
2.5
(e, 2e) cross section (a.u.)
Momentum (a.u.)

Fig. 8

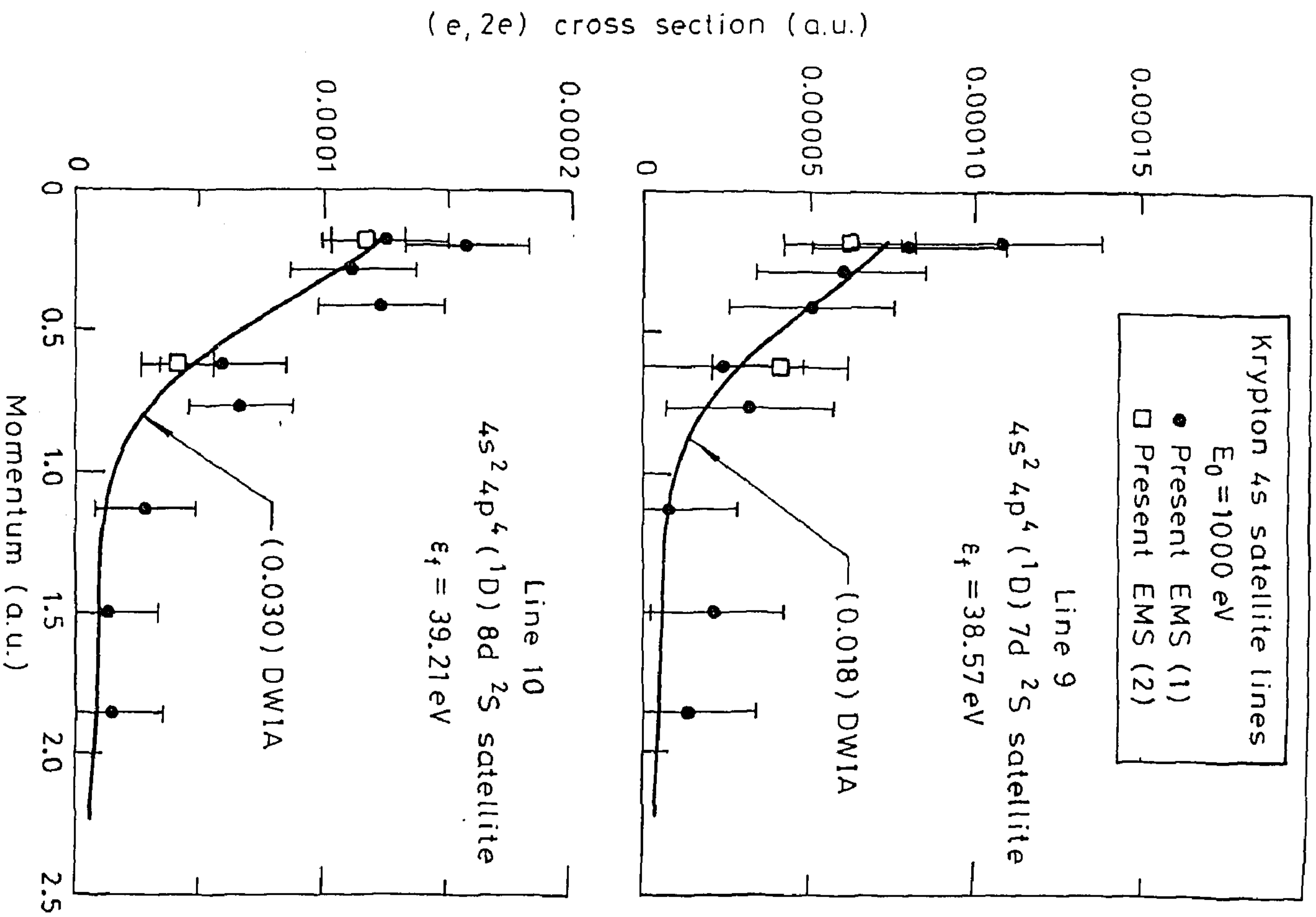
(e, 2e) cross section (a.u.)
0
0.00005
0.00010
0.00015
0
0.0001
0.0002
Krypton 4s satellite lines
E_0 = 1000 eV
● Present EMS (1)
□ Present EMS (2)
Line 9
$4s^2 4p^4 (^1D) 7d\ ^2S$ satellite
ε_f = 38.57 eV
(0.018) DWIA
Line 10
$4s^2 4p^4 (^1D) 8d\ ^2S$ satellite
ε_f = 39.21 eV
(0.030) DWIA
0
0.5
1.0
1.5
2.0
2.5
Momentum (a.u.)

Fig. 9

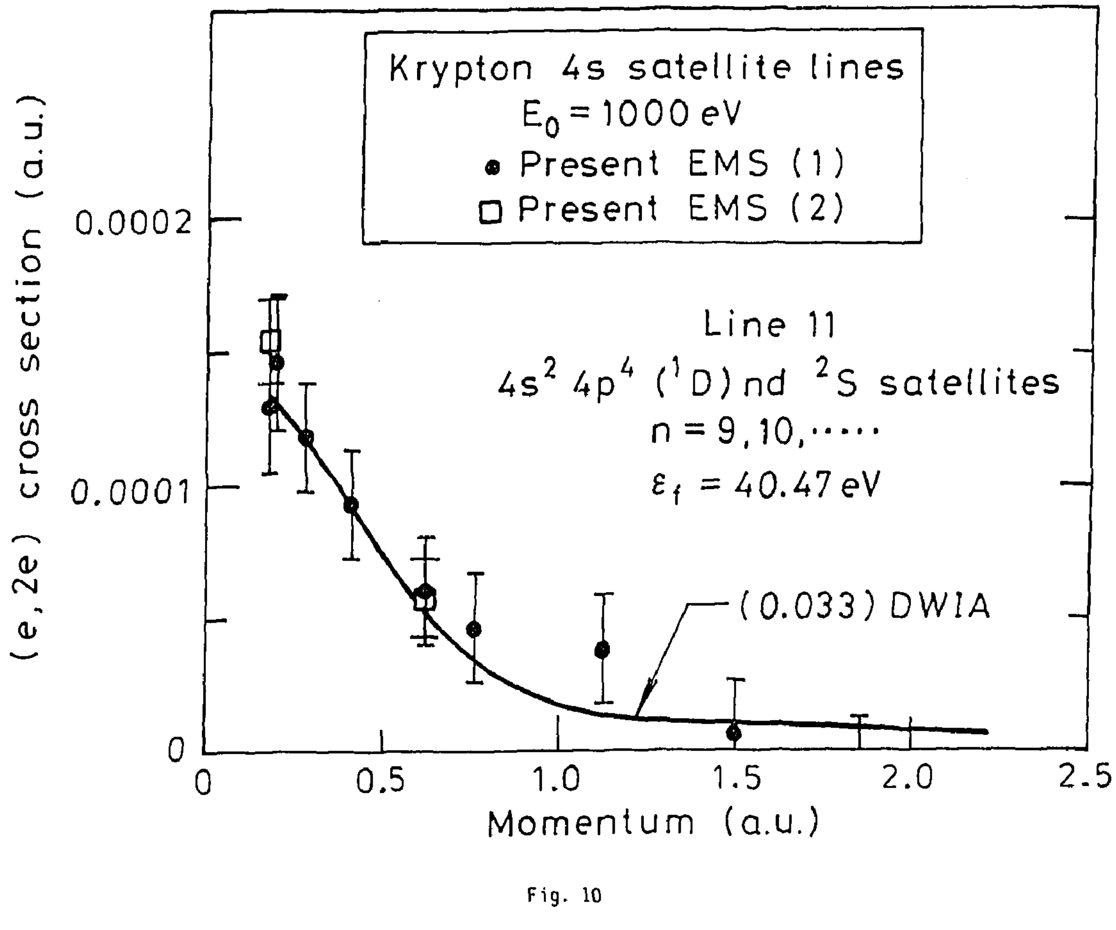
Krypton 4s satellite lines
E_0 = 1000 eV
● Present EMS (1)
□ Present EMS (2)
Line 11
$4s^2 4p^4 (^1D) nd\ ^2S$ satellites
n = 9, 10, ...
ε_f = 40.47 eV
(0.033) DWIA
(e, 2e) cross section (a.u.)
0.0002
0.0001
0
0
0.5
1.0
1.5
2.0
2.5
Momentum (a.u.)

Fig. 10

Table Captions

Table 1: Coefficients $c_{\alpha\beta}$ of basis orbitals in the 4*p* and 4*s* normalised Dyson orbitals of krypton.

Table 2: Spectroscopic factors and final-state configurations for the 4*p* and 4*s* manifolds of krypton as determined from the relative (e,2e) differential cross sections at 1000 eV. The one standard deviation error in the last significant figure is given in parentheses.

Table 1:

Basis	**4*p* orbital** coefficient	Basis	**4*s* orbital** coefficient
3*p*	-0.00725 ± 0.3452	3*s*	-0.0958 ± 0.0695
4*p*	0.9998 ± 0.0027	4*s*	0.9717 ± 0.0224
5*p*	-0.00162 ± 0.0048	5*s*	0.0614 ± 0.0194
6*p*	0.01895 ± 0.0028	6*s*	0.2069 ± 0.0460

Table 2 (continued):

Line	Binding Energy (eV)				Assignment $^{(a,b,c,e,f)}$	$S_i^{(a)}$					
	(a)	(b)	(c)	Present EMS		(a)	(c)	(d)	(e)	(g)	Present EMS
4*s* lines cont'd	36.47	36.47	34.78	36.47	$4s^24p^4(^1D)5d$ ^2P ^2S+$(^1D)6p$	0.07	0.084	-	0.089	0.13(2)	0.100(10)
		36.70			?	-	-	-	-	-	-
		37.65			?	-	-	-	-	-	-
	37.81	37.82	36.09	37.81	$4s^24p^4(^1D)6d$ ^2S	0.033	0.046	-	0.036	0.08(2)	0.027 (9)
	38.57	38.58	36.76	38.57	$4s^24p^4(^1D)7d$ ^2S	0.020	0.019	-	-	-	0.018 (9)
	39.21	39.04	37.26	39.21	$4s^24p^4(^1D)8d$ ^2S	-	0.005	-	-	-	0.030 (8)
	39.77	39.33	38.18	40.47	$4s^24p^4(^1D)nd, n \geq 9$ ^2S	0.011	0.014	-	-	-	0.033 (9)
		39.53									

(a) Svensson *et al.* ($h\nu$ = 1487 eV) [32]

(b) Krause *et al.* ($h\nu$ = 68.5 eV) [27]

(c) Fronzoni *et al.* [30] and Brosolo *et al.* [44]

(d) Fuss *et al.* [38]

(e) Dyall and Larkins [42, 43]

(f) Moore [50]

(g) Leung and Brion [39]

Table 2:

Line	Binding Energy (eV)				Assignment $^{(a,b,c,e,f)}$	$S_i^{(a)}$					
	(a)	(b)	(c)	Present EMS		(a)	(c)	(d)	(e)	(g)	Present EMS
4*p* lines											
$4p_{3/2}$	14.00	-	12.50	14.11	$4s^24p^5$ ^2P	0.964	0.910	~1	0.978	-	0.980 (5)
$4p_{1/2}$	14.67	-				-	-	-	-	-	-
4*s* lines											
	27.52	27.51	24.96	27.52	$4s^14p^6$ ^2S	0.658	0.564	0.46(2)	0.69	0.50(5)	0.510 (6)
		29.83		-	$(^1D)5s$ ^2D	-	-	-	-	-	-
	30.25	30.28		30.25	$4s^24p^4(^3P)4d$ ^2P	-	-	-	-	-	0.020 (10)
		30.69		-	$(^3P)4d$ $^2D_{3/2}$	-	-	-	-	-	-
		30.98		-	$(^3P)4d$ $^2D_{5/2}$	-	-	-	-	-	-
	31.25	31.29		-	$4s^24p^4(^3P)5p$ ^2P	0.011	0.006	-	0.002	-	-
		31.65	29.46	-	$(^3P)5p$ ^2S	-	-	-	-	-	-
	32.09	32.06	30.18	32.09	$4s^24p^4(^1S)5s$ ^2S	0.015	0.027	0.07(2)	0.024	0.06(2)	0.075 (5)
	32.75	32.61	30.98	-	$4s^24p^4(^1D)5p$ $^2P_{3/2,1/2}$	0.024	0.058	-	0.011	-	<0.005
		32.88		-		-	-	-	-	-	-
	33.98	33.96	32.54	33.98	$4s^24p^4(^1D)4d$ ^2S	0.157	0.196	0.20(2)	0.141	0.23(3)	0.202 (8)
		34.14		-	$(^3P)6s$ ^2P	-	-	-	-	-	-
		34.38		34.47	$(^1S)6s$ ^2S	-	-	-	0.013	-	0.029 (10)
	34.47		32.92	-	$4s^24p^4(^3P)6p$ ^2P	0.006	0.015	-	0.002	-	-
		34.74		-	?	-	-	-	-	-	-
	34.90	34.89	32.75	-	$4s^24p^4(^1S)5p$ $^2P_{1/2,3/2}$	0.006	0.001	-	0.003	-	-
		34.93				-	-	-	-	-	-
		35.14		-	?	-	-	-	-	-	-
		35.85		-	$(^1D)5d$ $^2D_{3/2}$	-	-	-	-	-	-
		36.12		-	$(^1D)5d$ $^2P_{1/2}$	-	-	-	-	-	-